Effects of current on early stages of focused ion beam nano-machining

Journal Item

Effects of current on early stages of focused ion beam nano-machining

Aydin Sabouri[1], Carl J Anthony[1], Philip D Prewett[2], James Bowen[3], Haider Butt[1]

[1]MicroEngineering and Nanotechnology group, School of Mechanical Engineering, University of Birmingham, Edgbaston, Birmingham, B15 2TT, UK
[2]Oxford Scientific Consultants Ltd, Abingdon. OX14 3SJ, UK
[3]School of Chemical Engineering, University of Birmingham, Edgbaston, Birmingham, B15 2TT, UK

Abstract

In this report we investigate the effects of focused ion beam (FIB) machining at low doses in the range of 10^{15} ions/cm^2 to 10^{16} ions/cm^2 for currents below 300 pA on Si(100) substrates. The effects of similar doses with currents in the range 10pA to 300 pA were compared. The topography of resulting structures has been characterized using atomic force microscope, while crystallinity of the Si was assessed by means of Raman spectroscopy. These machining parameters allow a controllable preparation of structures either protruding from, or recessed into, the surface with nanometre precision.

1. Introduction

Focused ion beams (FIB) are widely used as a tool for high precision material processing with unique capabilities in the micro and nanoscale regime. The FIB systems use a Liquid Metal Ion Source (LMIS) at the top of the column to produce the ions. Then the ions are extracted and focused by electric field. Finally they pass through apertures to adjust the beam current and scanned over the sample surface. Figure 1 shows the typical FIB column and its components.

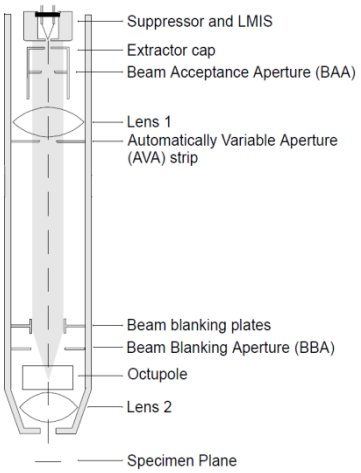

Figure 1. Focused ion beam column components [1]

The interaction of the energetic ions with the surface causes ion implantation and sputtering of substrate atoms thus modifying the surface. Moreover in addition to secondary electrons, from collection of backscattered ions, an image of the specimen surface can be constructed. Modern commercial systems can provide the beam for low currents (10pA) with an intensity profile of 10 nm full width at half maximum (FWHM) [1].

FIB systems are used frequently for device modifications [2], mask repair [3], transmission electron microscopy (TEM) sample preparation [4], Nano Electro Mechanical Systems (NEMS) prototyping [5] and as a direct-write mask tool in plasma etching process [6]. The main advantage of FIB is that it is a rapid dry technique, as compared to electron beam lithography and provide resistless fabrication method [7]. This is an outstanding capability as it wouldn't require planar surface for spinning the resist and machining would be possible on features which already etched.

FIB implantation, causes different types of damages to the substrate varying from formation of Frenkel pair to formation of amorphous layers in crystalline materials. These damages would alter the mechanical, electrical, chemical and optical behaviour of the material. For instance when FIB is used for thinning down the cantilevers which are used as AFM tip, it would change its mechanical characteristic. It was shown previously that FIB machining damage would have an important influence on quality factor of these structures [8;9]. The effects of ion implantation on properties of material have been investigated previously by various studies [10-12].

In FIB machining, generally the depth of milling is identified by dose of ion implantation. However in order to use FIB more effectively, it is required to investigate the effect of current along with the implantation dose in order to achieve controllable milling with nanometre precession.

Huey et al. have reported the characterization of features fabricated by FIB at doses below 10^{16} ions/cm^2 illustrating the surface topography of FIB exposed area by means of AFM measurements [13]. They found that by varying the implantation dose from 10^{13} to 10^{17} ions/cm^2, either protruding from, or recessed into the surface occurs.

In this paper we are investigating the effect of machining current on sputtering rate and Si structure at doses in the range 10^{15} - 10^{16} ions/cm^2, normally associated with the early stages of milling. Since the threshold of milling is within this range, investigation of these doses would provide the nanometre milling precision. Moreover, the FIB implantation masking behaviour is started from 10^{15} ions/cm^2 and altering the damage would provide

different masking behaviour. For investigation of topographical changes of the processed areas, AFM measurements were performed. Raman spectroscopy was employed to verify the crystallinity of Si after milling at different currents.

2. Theory

In FIB machining the collision between ion and substrate induces secondary processes such as recoil and sputtering of constituent atoms, defect formation, electron excitation and emission, and photon emission [14]. Ion implantation is a key technique which is used for material modification during fabrication of semiconductors. The implantation in FIB machining is undesirable due to the resultant change in material structure. However, sometimes this focused implantation can be used effectively in changing the dopant of semiconductors [15]. For modelling ion implantation, the Gaussian distribution function can be employed to predict the probability of obtaining an ion at distance *z* beneath the surface [16].

$$\frac{dN(z)}{N} = f(z)dz = Ke^{\frac{-(z-R_p)^2}{2\sigma^2}}dz \qquad (1)$$

Where *N* is the number of ions arriving at the surface in *t* seconds, R_p the mean projected range and σ is standard deviation. The constant *K* may be calculated from the normalisation equation

$$\int_{-\infty}^{\infty} Ke^{\frac{-(z-R_p)^2}{2\sigma^2}}dz = 1 \qquad (2)$$

which leads to,

$$K = \frac{\sqrt{2}}{\sigma\sqrt{\pi}\,\mathrm{erf}\left(\frac{Rp}{\sqrt{2}\sigma}\right)} \qquad (3)$$

Therefore the density distribution in a time interval $t \to t + dt$ from eq.1 can be written as

$$\frac{dN(z)}{dt} = \frac{I}{eA}.K.e^{\frac{-(Rp-z)^2}{2\sigma^2}} \qquad (4)$$

Where $e=1.6\times10^{-19}$ *C*, *I* is the milling current (pA) and *A* is the pattern area (μm^2).

The dominant effect in FIB milling is sputtering which causes the datum position of the Gaussian implantation profile to move into the sample at a constant rate as the top surface is removed. The net ion distribution as a function of the depth *x* below the resultant etched surface after *t* seconds is a sum of shifted Gaussians, resulting in an asymmetrical ion density distribution *n(x)* of form:

$$v(\varepsilon) = \frac{\mathrm{erf}\left(\frac{\varepsilon-1+X'}{\delta\sqrt{2}}\right)-\mathrm{erf}\left(\frac{\varepsilon-1}{\delta\sqrt{2}}\right)}{1+\mathrm{erf}\left(\frac{1}{\delta\sqrt{2}}\right)} \qquad (5)$$

The normalized variables are

$$v(\varepsilon) = \frac{n(\varepsilon)}{\frac{\rho}{YM}}; \qquad \varepsilon = \frac{x}{R_p}; \qquad \delta = \frac{\sigma}{R_p}$$

Where ρ is the density of the substrate material, *M* is the atomic mass of the constituent atoms, *Y* is the sputter rate of atoms per ion, *x* is depth below the etched surface and X′ is the normalised etch depth which is given by $X' = \frac{X}{R_p}$. The final datum position after an etch time *t* is the etch depth X=*at*, where

$$a = \frac{MYI}{eA\rho} \qquad (6)$$

is the material removal rate in m/s.

The form of this implanted ion profile is shown in Fig. 2. The values for R_p and σ are calculated as 27 nm and 9 nm respectively for 30 keV ion implantation [17].

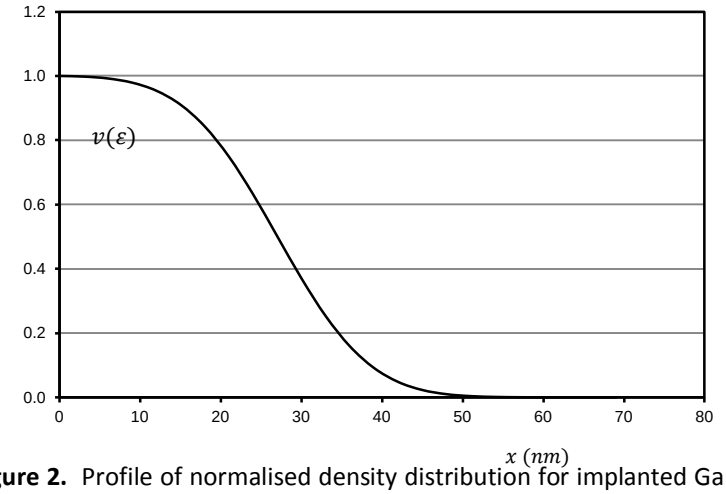

Figure 2. Profile of normalised density distribution for implanted Ga ions into the Si. For an etch depth of 55 nm, X′ is 2.06 and δ is 0.33

3. Experimental

A Strata DB235 dual-beam FIB/SEM machine (FEI, UK) was used in order to modify the surface of Si(100) wafers (n-doped from Si-Mat). This FIB system uses liquid Ga as an ion source, the emission current was 2.2 µA and after extraction the ions were accelerated to the energy of 30 keV for all the reported experiments. The sample chamber pressure was 1.4×10^{-9} bar. A dwell time of 100 ns and a 50 % overlap were used for beam during the performed machining. For milling, the pixel size is calculated by dividing the full length of the image by 4096, the number of pixels along that axis. The magnification was set to 2500X in the field of view, which was approximately 120 µm × 120 µm; consequently the pixel-to-pixel distance is 29 nm. In addition to an ion microscope the system has a field emission gun electron microscope which provides investigation of surfaces without unintentional ion implantation; this was used to determine the milled area, an example of which is shown in Fig. 3.

The FIB spot size is mainly dependent on the beam current, which is filtered by an appropriate aperture. By increasing the current the spot size is increased (Table 1) which also implies a wider beam tail [18;19].

Table 1. Beam currents and corresponding milling spot size [1]

Beam Current (pA)	**Milling spot size (nm)**
10	10
50	15
100	20
300	25

Doses in the range 10^{15} - 10^{16} ions/cm^2 were exposed by repeated scans of 30 µm × 30 µm squares, using ion beam currents varying from 10 pA to 300 pA (Fig. 3(a)). The doses, corresponding currents, and exposure times were calculated using eq. 7, where *D* is the exposure dose in ions/cm^2 and *t* is exposure time in s. Table 2 shows the relevant milling times for corresponding doses and currents.

$$D = \frac{I_{ion}\ t_{exposure}}{1.602 \times 10^{-15} A} \qquad (7)$$

Table 2. Corresponding time for different doses and currents

Dose (ions/cm^2) Current (pA)	**1×10^{15}**	**2×10^{15}**	**4×10^{15}**	**1×10^{16}**
10	144 s	288 s	576 s	1441 s
50	28 s	57 s	115 s	288 s
100	14 s	28 s	57 s	144 s
300	4 s	9 s	19 s	48 s

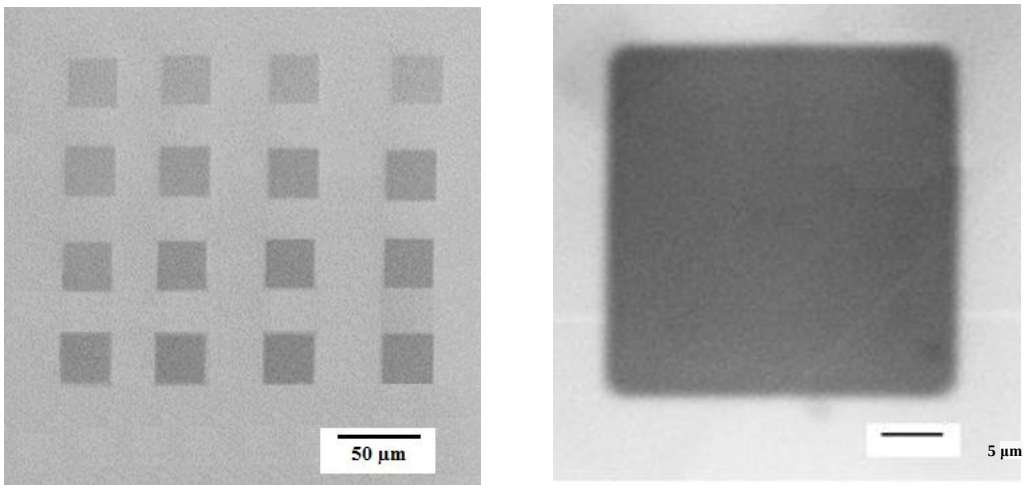

Figure 3. (a) SEM micrograph of milled area. Columns milled by the same total number of ions with different machining current (milling parameters defined in table 2) (b) Magnified SEM image of the milled region.

Topographies of the implanted areas were acquired using a NanoWizard II atomic force microscope (JPK Instruments, UK) operating in intermittent contact mode at a tip velocity of 2 µm/s, employing pyramidal tipped Si cantilevers (PPP-NCL, Windsor Scientific, UK). For investigation of the Si crystallinity, Raman measurements using a Renishaw Raman Microscope with 514 nm laser edge, 1800 I/mm grating and a laser power of 0.36 mW was used. The measurements were obtained by averaging three scans with a mean wavenumber resolution of 1.5 cm^{-1}.

In Raman measurements crystalline Si and amorphous Si are identified from their unique peak in the Raman spectrum. Moreover the intensity of peaks qualitatively illustrates the amount of each material present. A typical Raman spectrum with a composition of crystalline silicon (peak centre 520 cm^{-1}) and amorphous silicon (peak centre 470 cm^{-1}) is shown in Fig. 4.

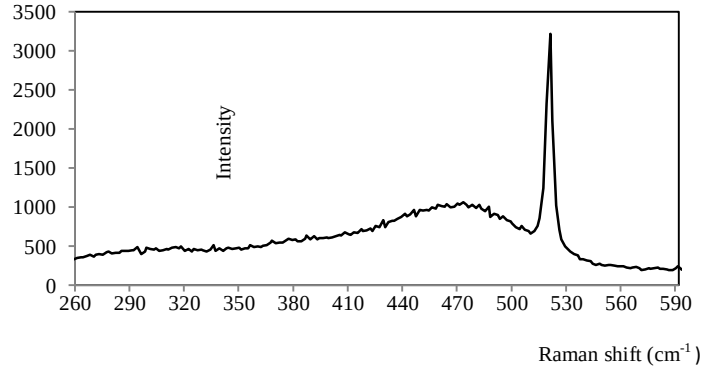

Figure 4. Typical Raman spectrum for crystal Si (sharp peak 520 cm^{-1}) and amorphous Si (broad peak 470 cm^{-1})

4. Results and Discussion

The 3D images of FIB milled squares measured using AFM for doses of 10^{16} ions/cm^2 at currents of (a) 10 pA and (b) 300 pA are shown in Fig. 5. These plots were used to determine the average mill depth by comparing with the surrounding un-milled silicon region.

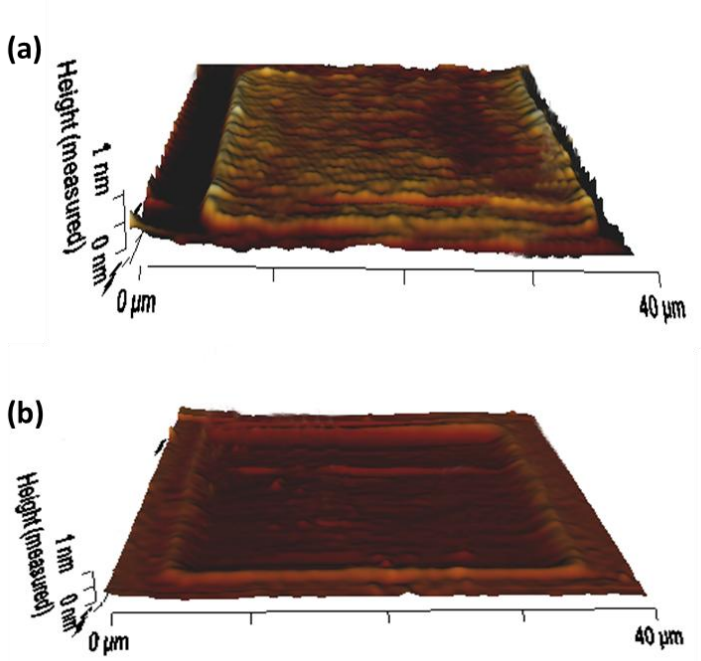

Figure 5. (a) AFM topography of a swollen exposed Si surface after FIB machining at a dose of 10^{16} ions/cm^2 with current 10 pA. (b) AFM topography of a processed Si surface for a dose of 10^{16} ions/cm^2 with current 300 pA.

The results of the mill depth obtained from the AFM topography measurement data after milling are shown in Figure 5, where positive depth means the processed area is protruding from the original surface. It was observed that for all doses below 10^{16} ions/cm^2, surface swelling occurred. The surface swelling is believed to occur in order to relieve strain caused by implanted Ga ions [8] as well as sub surface damage [20]. By increasing the current at corresponding doses a reduction in surface swelling, which could be the indicative of greater removal of substrate material, was also observed (Fig. 6). At a dose of 10^{16} ions/cm^2 it was seen that for currents above 50 pA "net material sputtering" occurred and the surface topography of the milled area was below the original Si surface height. Increasing the current for constant dose would increase the number of ions delivered into the surface per unit time; however the total number of ions arriving at the surface remains the same.

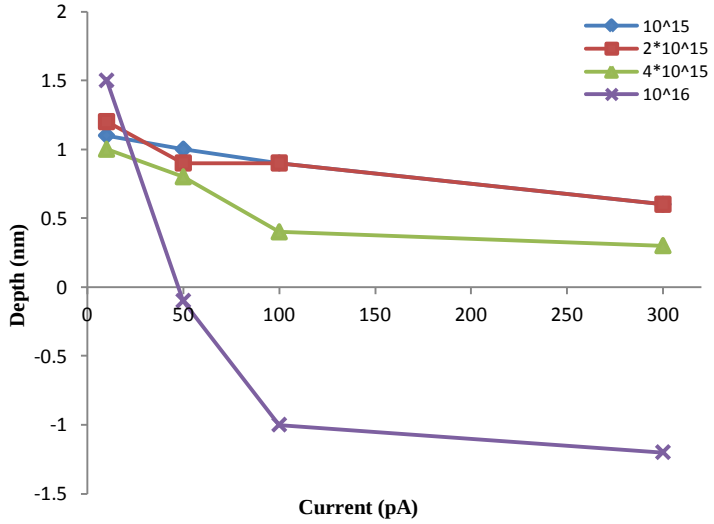

Figure 6. Depth of processed area at different doses

The same milled regions were analysed by means of Raman spectroscopy to investigate the silicon lattice structure. A reference measurement was performed on virgin surface and the crystalline Si peak was observed at

a wavenumber of 520 cm^{-1}. For milled areas, spectra similar to Fig. 4 were observed, revealing a broad peak with centre 470 cm^{-1}. Figs 7(a) and 7(b) show the intensity ratios of crystalline Si peak to amorphous Si peak for the exposed areas. Higher values indicate more crystalline Si in the lattice. However there is not a direct linear relation between peak ratio and amorphous/crystalline Si ratio in the implanted layer. The Raman spectrometer with the wavelength of 514 nm samples to a depth of approximately 700 nm in Si and so samples the underlying substrate as well as the damaged surface layer. As the thin amorphous layer absorbs the Raman light, so the amount of signal coming from the underlying Si reduces with increasing amorphous content of the layers. Thus the peak ratio can be used to see the trend of how the amorphous content of the layer changes with milling conditions. Besides lowering the intensity of crystal peak, additional modes also are appeared in spectrum in the form of broad-bands at lower frequencies which is originated from the amorphous region.

Fig. 7(a) illustrates that increasing the dose would increase the Si damage for all currents which indicates greater disorder. It also shows that there is an asymptotic behaviour of the peak ratio with dose implying that the damage is continuously increasing before milling starts; this level of damage is then maintained in the implanted surface layer as it moves with the etched surface. Fig. 7(b) shows that for currents of 100 pA and greater the peak ratio remains almost constant. By starting net material removal, the intensity ratios between crystal Si and amorphous Si tend to remain constant, which implies that it is reaching the saturation state [21]. A noteworthy observation is that there is no difference in form of the ratio vs. current plots for the different doses, as shown in Fig. 7(b), unlike the height data given in Fig. 6; only a difference in magnitude is observed.

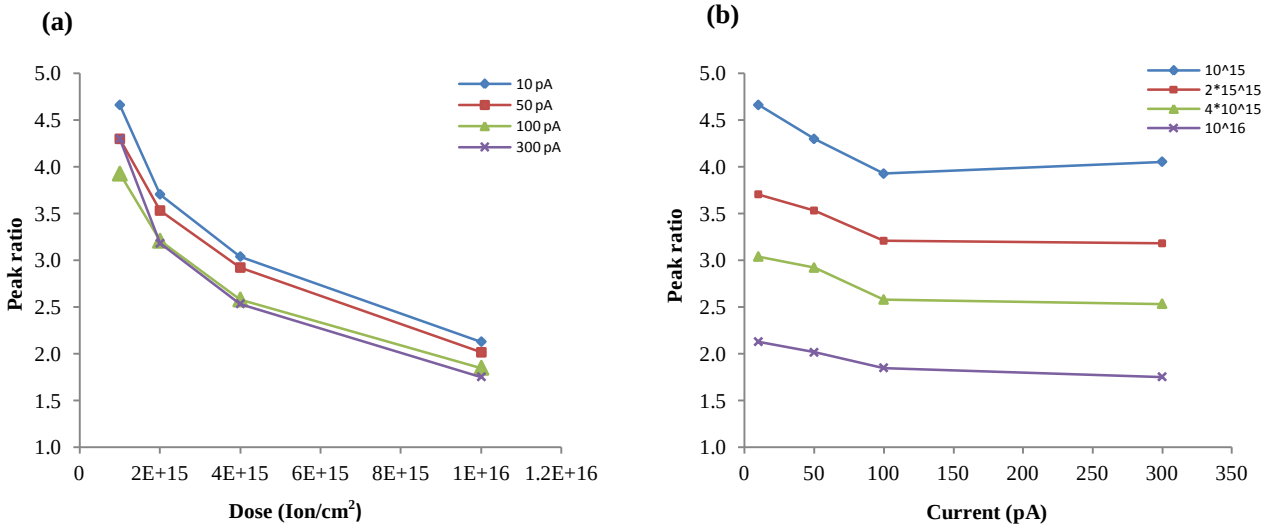

Figure 7 (a). Raman peak ratio trend for same current at different doses (b). Raman peak ratio for same doses at different currents

In order to find the effective flux of ion implantation at different currents the following manner is used. For a single ion impact the lateral cross section σ_0 of a region with a significant primary defect production is calculated using eq. 8:

$$\sigma_0 = \frac{S_n}{E_c} \qquad (8)$$

Where S_n and E_c are the nuclear stopping cross sections and the critical nuclear deposition; E_c is lower than nominal displacement threshold E_d as the substrate is no longer perfect crystal. This value can be assumed to be $E_c=E_d/4$, therefore the value of E_c is 3.75eV [22].

The average time for consecutive ion impact into the same region is calculated using eq. 9.

$$\tau_i = \frac{1}{\dot{D}\sigma_0} \qquad (9)$$

Where $\dot{D}$ is the nominal ion flux; therefore, τ_i would be in the range of micro-seconds for used milling currents [22]. Therefore, the overlap of regions with defects produced by different ions is not probable with the studied currents. Also in this process the effect of temperature rise is negligible as it is less than 2 degrees [18].

Tian et al. [23] reported the impurity profile of implantation into Si by using a Rutherford backscattering experiment. It has been shown that higher currents produce shallower channelling tails than do the lower beam current due to de-channelling. Since the total number of implanted ions is same at all milling currents, shallower implantation depths leads to the higher atomic density at the regions closer to the surface which would increase the collisions between implanted ions and substrate atoms. Consequently for higher currents, more energy deposition close to the surface is occurred which causes more sputtering. In addition, the Raman characterization has shown that higher currents cause more damage to substrate (Fig 7b). This means that for higher currents at low doses more amorphous layers are produced. Hence for the same energy deposited to the Si, the probability of sputtering is increasing, as in amorphous layers the displacement energy is lower compared to crystalline Si [22]. In this process the effect of temperature rise is negligible as it is less than 2 ^{o}C [24].

5. Conclusion

In FIB machining low currents are used for imaging and for high resolution machining due to lower sputtering rate and finer beam spot size. Using low currents is not an effective way to accomplish high dose milling as it takes a long time to perform. However, combining doses close to the sputtering threshold with low currents enables us to use the FIB as a tool in order to perform direct pattern lithography and nanometre resolution machining. Also it was shown by previous studies that these low implantation doses can successfully act as a hard mask in wet and dry etching [25]. The masking behaviour is mainly due to induced strain caused by ion implantation damage in substrate [6;26]. This study suggests that apart from implantation dose which has been considered as a main parameter, the milling current can have an important effect on masking behaviour of implanted regions and could alter etching selectivity which is needed to be investigated in further studies.

In this report surface topography and the change in lattice structure of Si(100) has been characterized for the first time at the early stages of FIB machining at various currents. It is conjectured that the dose rate effects could be responsible for significant effects on nanoscale machining causing variations from swelling to milling at low doses. Moreover, by comparing the Raman spectrum peaks for crystal and amorphous silicon, it was revealed that lower currents cause less damage for corresponding doses from Raman measurements.

6. Acknowledgement
The research leading to these results has received funding from the European Union's Seventh Framework Programme FP7/2007-2013 under Grant Agreement No. 318804 (SNM: Single Nanometer Manufacturing for beyond CMOS devices).

The Atomic Force Microscope used in this research was obtained, through Birmingham Science City: Innovative Uses for Advanced Materials in the Modern World (West Midlands Centre for Advanced Materials Project 2), with support from Advantage West Midlands (AWM) and part funded by the European Regional Development Fund (ERDF).

HB thanks Philip Leverhulme Trust for the grant funding.

7. References

[1] "*FEI xP DualBeam Workstation, xPDB Manual Set: PN25421-A*," 2001.

[2] Y. Chen and X. Zhang, "Focused Ion Beam Technology and Application in Failure Analysis," *2010 11Th International Conference on Electronic Packaging Technology & High Density Packaging (Icept-Hdp)*, pp. 957-960, 2010.

[3] P. D. Prewett and P. J. Heard, "Repair of Opaque Defects in Photomasks Using Focused Ion-Beams," *Journal of Physics D-Applied Physics*, vol. 20, no. 9, pp. 1207-1209, 1987.

[4] F.A Stevie, L.A Giannuzzi, and B.I Prenitzer, *INTRODUCTION TO FOCUSED ION BEAM- Instrumentation, Theory, Techniques and Practice* Springer, 2005.

[5] S. C. Charandabi, P. Prewett, C. Hamlett, C. Anthony, and J. Preece, "Nano planar coil actuated micro paddle resonator for mass detection," *Microelectronic Engineering*, vol. 88, no. 8, pp. 2229-2232, 2011.

[6] N. Chekurov, K. Grigoras, A. Peltonen, S. Franssila, and I. Tittonen, "The fabrication of silicon nanostructures by local gallium implantation and cryogenic deep reactive ion etching," *Nanotechnology*, vol. 20, no. 6 2009.

[7] D. Petit, C. C. Faulkner, S. Johnstone, D. Wood, and R. P. Cowburn, "Nanometer scale patterning using focused ion beam milling," *Review of Scientific Instruments*, vol. 76, no. 2 2005.

[8] P. Prewett, C. Anthony, D. Cheneler, and M. Ward, "Stress-induced curvature of focused ion beam fabricated microcantilevers," *Micro & Nano Letters*, vol. 3, no. 1, pp. 25-28, 2008.

[9] C. Anthony, G. Torricelli, P. Prewett, D. Cheneler, C. Binns, and A. Sabouri, "Effect of focused ion beam milling on microcantilever loss," *Journal of Micromechanics and Microengineering*, vol. 21, no. 4 2011.

[10] B. Naydenov, V. Richter, J. Beck, M. Steiner, P. Neumann, G. Balasubramanian, J. Achard, F. Jelezko, J. Wrachtrup, and R. Kalish, "Enhanced generation of single optically active spins in diamond by ion implantation," *Applied Physics Letters*, vol. 96, no. 16 2010.

[11] Y. J. Li, F. Machalett, S. Linzen, F. Schmidl, and P. Seidel, "Transport Characteristics and Structural-Analysis of Yba2Cu3O7-X Thin-Films Implanted with Argon Ions," *Physica Status Solidi A-Applied Research*, vol. 147, no. 1, pp. 119-128, 1995.

[12] R. Ross and M. T. Pham, "Modification of the Chemical Properties of Silicon by Ion-Implantation with High-Doses of Ar and P," *Journal of Radioanalytical Chemistry*, vol. 50, no. 1-2, pp. 45-52, 1979.

[13] B. D. Huey and R. M. Langford, "Low-dose focused ion beam nanofabrication and characterization by atomic force microscopy," *Nanotechnology*, vol. 14, no. 3, pp. 409-412, 2003.

[14] Nan Yao, *Focused ion beam systems basic and application* Cambridge, 2007.

[15] S. D. Chu, J. C. Corelli, A. J. Steckl, R. H. Reuss, W. M. Clark, D. B. Rensch, and W. G. Morris, "Comparison of Npn Transistors Fabricated with Broad Beam and Spatial Profiling Using Focused Beam Ion-Implantation," *Journal of Vacuum Science & Technology B*, vol. 4, no. 1, pp. 375-379, 1986.

[16] P.D.Prewett and G.L.Mair, *Focused ion beams from liquid metal ion sources* Research Studies Press, 1991.

[17] P. D. Prewett and G. M. Sundaram, "Focused Ion-Beam Repair - Staining of Photomasks and Reticles," *Journal of Physics D-Applied Physics*, vol. 26, no. 7, pp. 1135-1137, 1993.

[18] J. W. Ward, M. W. Utlaut, and R. L. Kubena, "Computer-Simulation of Current-Density Profiles in Focused Ion-Beams," *Journal of Vacuum Science & Technology B*, vol. 5, no. 1, pp. 169-174, 1987.

[19] L. Wang, "Design optimization for two lens focused ion beam columns," *Journal of Vacuum Science & Technology B*, vol. 15, no. 4, pp. 833-839, 1997.

[20] O. Ertl, L. Filipovic, and S. Selberherr, *Three-Dimensional Simulation of Focused Ion Beam Processing Using the Level Set Method* 2010, pp. 49-52.

[21] F. A. Trumbore, "Solid Solubilities of Impurity Elements in Germanium and Silicon," *Bell System Technical Journal*, vol. 39, no. 1, pp. 205-233, 1960.

[22] M. Posselt, L. Bischoff, D. Grambole, and F. Herrmann, "Competition between damage buildup and dynamic annealing in ion implantation into Ge," *Applied Physics Letters*, vol. 89, no. 15 2006.

[23] S. Tian, S. H. Yang, S. Morris, K. Parab, A. F. Tasch, D. Kamenitsa, R. Reece, B. Freer, R. B. Simonton, and C. Magee, "An Examination of the Effect of Dose-Rate on Ion-Implanted Impurity Profiles in Silicon," *Journal of the Electrochemical Society*, vol. 142, no. 9, pp. 3215-3219, 1995.

[24] C. A. Volkert and A. M. Minor, "Focused ion beam microscopy and micromachining," *Mrs Bulletin*, vol. 32, no. 5, pp. 389-395, 2007.

[25] Z. J. Liu, K. Iltanen, N. Chekurov, K. Grigoras, and I. Tittonen, "Aluminum oxide mask fabrication by focused ion beam implantation combined with wet etching," *Nanotechnology*, vol. 24, no. 17 2013.
[26] H. Qian, X, W. Zhou, J. Miao, L. E. Lim, and X. Zeng, "Fabrication of Si microstructures using focused ion beam implantation and reactive ion etching," *Journal of Micromechanics and Microengineering*, vol. 18, no. 3 2008.